

Article

Tuning the Architecture of Hierarchical Porous CoNiO₂ Nanosheet for Enhanced Performance of Li-S Batteries

Lili Chai , Huizi Ye, Zhengguang Hu, Fengliang Liu, Liyun Qin, Zhiqi Zhang, Xianxin Lai, Yong Zhao * and Li Wang *Department of Physics, School of Physics and Materials Science, Nanchang University, Nanchang 330031, China
* Correspondence: zhaoyong@ncu.edu.cn (Y.Z.); liwang@ncu.edu.cn (L.W.)

Abstract: As the desired components and crystal structure of a transition metal oxide catalyst are selected, architecture is a dominating factor affecting its electrocatalytic performance for applications in lithium-sulfur (Li-S) batteries. Nano-compounds with a hollow architecture are undoubtedly the ideal catalysts for enhancing cathodic performance for more exposed active sites and shortened path lengths than are other architectures. Additionally, the internal stress in hollow architecture is favorable for further performance enhancement, due to its regulation effects of driving the d-band center of the transition metal in the active sites to migrate toward the Fermi level, which will promote the chemical adsorption and catalytic conversion of the polysulfides (PSs). To this point, we select hierarchical porous dual transition metal oxide CoNiO₂ nano-boxes (CoNiO₂(B)) as the conceptual model; meanwhile, CoNiO₂ nano-flakes (CoNiO₂(F)) with identical stoichiometry and crystal structure are also analyzed as a comparison. Li-S batteries based on CoNiO₂(B) deliver superior energy storage features, including a reversible discharge capacity of 1232 mAh g⁻¹ at 0.05 C and a stable cycle performance with decay rate of 0.1% each cycle even after 300 cycles at 1 C. This research presents an alternative scheme for booting the performance of Li-S batteries.

Keywords: transition metal oxide; hollow architecture; catalysis; Li-S battery



Citation: Chai, L.; Ye, H.; Hu, Z.; Liu, F.; Qin, L.; Zhang, Z.; Lai, X.; Zhao, Y.; Wang, L. Tuning the Architecture of Hierarchical Porous CoNiO₂ Nanosheet for Enhanced Performance of Li-S Batteries. *Batteries* **2022**, *8*, 262. <https://doi.org/10.3390/batteries8120262>

Academic Editors: Yuanhua Xiao, Ling Wu, Xianwen Wu and Yiping Tang

Received: 19 October 2022

Accepted: 25 November 2022

Published: 29 November 2022

Publisher's Note: MDPI stays neutral with regard to jurisdictional claims in published maps and institutional affiliations.



Copyright: © 2022 by the authors. Licensee MDPI, Basel, Switzerland. This article is an open access article distributed under the terms and conditions of the Creative Commons Attribution (CC BY) license (<https://creativecommons.org/licenses/by/4.0/>).

1. Introduction

Li-S batteries are generally accepted as the most attractive energy storage systems owing to their high specific capacity of 1675 mAh g⁻¹ and theoretical energy density of 2600 Wh kg⁻¹ [1,2]. Additionally, as an active substance, sulfur is ample on Earth and environmentally friendly [3,4]. However, several technical issues, including the intrinsic insulating properties of sulfur, the shuttle effect associated with soluble PSs, and the enormous variation in volume during electrochemical reaction, significantly constrain the industrial application of Li-S batteries [5,6].

In the last few decades, many kinds of sulfur hosts have been developed to tackle the problems mentioned above. Among each host, conductive porous carbon has been considered the most promising material [7–9]. The porous carbon host greatly increases the sulfur cathode's electronic conductivity as well as provides sufficient empty space to contain volumetric alterations during charging and discharging reactions [10–12]. Nazar et al. prepared mesoporous carbon with a highly organized structure (CMK-3), and the S/CMK-3 cathode had a high initial capacity of 1005 mAh g⁻¹ at sulfur loads of up to 70 wt% [13]. Despite the fact that their initial cycle-specific capacities for carbon/sulfur composites are extraordinarily high, capacity decays sharply in later cycles due to the repulsion between polar PSs and non-polar carbonaceous substrates.

In recent years, polar non-organic substances such as transition metal oxides [14–17], sulfides [18–20], carbides [21,22], and hydroxides [23,24] have been focused on effective sulfur hosts, which are not only an effective component to chemically capture lithium polysulfide (LiPSs) but also an excellent catalysis for facilitating LiPSs conversion kinetics [25].

Among them, the layered double hydroxides (LDHs) and their derived oxide are a class of prominent sulfur hosts. The abundant hydrophilic groups in LDHs have strong affinity for LiPSs, and the existence of numerous sulfophilic sites accelerates the transformation kinetics of LiPSs [26,27]. As the desired components and crystal structure are selected, architecture-tuning is another key factor affecting the electrocatalytic performance of the material. Nanostructures with hollow architecture, including nano-boxes, nano-cages, and hollowed-spheres, etc., are undoubtedly a series of ideal configuration in enhancing catalytic performance, exhibiting more exposed active sites than other morphological structures. Furthermore, tensile strain aroused from the smaller curvature radius in hollow architecture is another effective factor in performance enhancement, as the tensile strain regulates the electronic structure of materials and drives the d-band center of the transition metal in the active sites to migrate toward the Fermi level, which will enhance the chemical adsorption and catalytic conversion of the PSs [28,29]. Benefiting from multivariate designable morphologies and controllable synthesis, metal-organic frameworks (MOFs) are desired sacrificial templates for synthesis of hollowed-LDH-nanostructures. Through annealing at appropriate temperature, they can further be transformed to oxide-hollowed analogues. Due to the high aspect ratio and hierarchical porous structure inherited from MOFs, these hydroxide- or oxide-hollowed nanostructures are especially favorable for improving utilization of a sulfur cathode. For example, Zhao's group prepared a hollow-structured NiCo-LDH, and the corresponding Li-S battery exhibited excellent capacity (1540 mAh g^{-1} at 0.1 C) and a high rate of electrical performance (485 mAh g^{-1} at 5.0 C) [30]. Ying et al. developed a MnO-TiO₂ core-shell nano-box composite with a 0.05% decay rate each cycle after 500 cycles at 0.5 C [31]. These transition metal hydroxide and oxide sulfur hosts grown on MOFs exhibit extraordinary electrochemical activity for Li-S batteries.

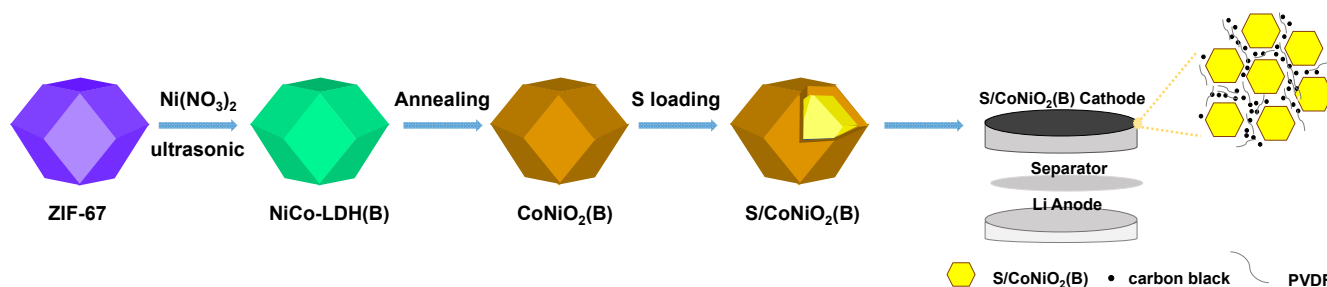
Given its low cost and inherent corrosion resistance, bimetallic nickel cobalt oxide has great advantages as an excellent catalyst with dual roles for accelerating the slow redox kinetics [32]. In this paper, we adopt dual transition metal oxide CoNiO₂(B) with a hierarchical porous structure as the conceptual model and CoNiO₂(F) with identical stoichiometry and crystal structure as the comparative control sample. CoNiO₂(B) was transformed from ZIF-67 through the ultrasonic solve-thermal method. The Li-S battery based on CoNiO₂(B) delivers outstanding energy storage features, including a reversible discharge capacity of 1232 mAh g^{-1} at 0.05 C, and a stable cycle performance with a decay rate of 0.1% each cycle even after 300 cycles at 1 C.

2. Results and Discussion

The preparation process of the S/CoNiO₂(B) cathode is schematically illustrated in Scheme 1. First, ZIF-67 is used as a sacrificial template. When nickel nitrate is added, ZIF-67 is etched by H⁺, which is produced by the hydrolysis of Ni²⁺. Then, the -NH₂ falls off from ZIF-67 under ultrasonic vibration and hydrolyzes to generate OH⁻, which accelerates the internal collapse of ZIF-67 and causes Co²⁺ to move outward. Both free Co²⁺ and Ni²⁺ bind with OH⁻ and co-deposit on the surface of the ZIF-67 framework to form NiCo-LDH nanosheets [33], which finally stack together to constitute a hollow NiCo-LDH nano-box (NiCo-LDH(B)). With further annealing, NiCo-LDH(B) is transformed into CoNiO₂(B). Sulfur is injected into CoNiO₂(B) by the melt-diffusion method; finally, formed S/CoNiO₂(B), carbon black, and PVDF are mixed as the cathode to assemble the Li-S battery.

Figure 1a is the scanning electron microscope (SEM) picture of ZIF-67. It can be observed that the formed ZIF-67 template exhibits a regular dodecahedron morphology. NiCo-LDH(B) (Figure 1b) constructed with nanosheets presents a hollow nano-box shape with uniform size. The finally transformed CoNiO₂(B) in Figure 1c has almost the same regular polyhedral morphology as ZIF-67. By thermal removal of crystal water in NiCo-LDH nano-flakes (NiCo-LDH(F)) (Figure 1d) synthesized by hydrothermal procedure, CoNiO₂(F) is also prepared as the comparative sample, whose two-dimensional morphology is inherited from NiCo-LDH(F), as shown in Figure 1e. Transmission electron

microscopy (TEM) was employed to further analyze the morphology and crystal structure of the transition metal oxide nano-boxes and nano-flakes. The TEM image of $\text{CoNiO}_2(\text{F})$ (Figure 1f) verifies the perfect crystallinity, and its inset exhibits distinct lattice fringes with a spacing of 0.24 nm corresponding to the (200) plane of CoNiO_2 . The transmission electron microscope image of $\text{CoNiO}_2(\text{B})$ (Figure 1g) illustrates the hollow interior. Figure 1h is a high-magnification TEM image of $\text{CoNiO}_2(\text{B})$, which indicates two set lattice fringes, with interplanar spacings of 0.24 and 0.21 nm, which correspond to the (200) and (111) planes of the CoNiO_2 compound crystal, respectively. Figure 1f is the EDS mapping of $\text{CoNiO}_2(\text{B})$, which displays the uniform elemental distribution of the Ni, Co, and O components.



Scheme 1. Scheme of the synthesis of the $\text{CoNiO}_2(\text{B})$, $\text{S/CoNiO}_2(\text{B})$, and $\text{S/CoNiO}_2(\text{B})$ cathode.

X-ray diffraction (XRD) measurements were conducted to investigate the crystallographic characteristics of the materials. Diffraction peaks of $\text{NiCo-LDH}(\text{B})$ in Figure 2a were located at $2\theta = 11.2^\circ$, 22.3° , 34.1° , and 62.8° , corresponding to the (003), (006), (012), and (110) planes, respectively, of a standard NiCo-LDH crystal [34]. The two materials of $\text{CoNiO}_2(\text{B})$ and $\text{CoNiO}_2(\text{F})$ have identical XRD diffraction patterns as shown in Figure 2b. The diffraction peaks at 36.8° , 42.8° , 61.8° , 73.9° , and 77.9° exactly fit in with the crystal planes (111), (200), (220), (311), and (222), respectively, of the standard CoNiO_2 bulk crystal (PDF#10-0188). Raman spectra also verified the detection results of XRD, as displayed in Figure 2c. $\text{CoNiO}_2(\text{B})$ and $\text{CoNiO}_2(\text{F})$ have two obvious Raman spectra peaks at 494 cm^{-1} and 1061 cm^{-1} , which correspond to the fingerprint Raman peaks of CoNiO_2 oxide compounds. After vulcanization, the Raman peak position of $\text{S/CoNiO}_2(\text{B})$ and $\text{S/CoNiO}_2(\text{F})$ remains unchanged, and the peak intensity becomes weak. The results of XRD diffraction and Raman characterization confirm that the two CoNiO_2 nano-compounds have the identical crystal structures. In Figure 2d, $\text{S/CoNiO}_2(\text{B})$ and $\text{S/CoNiO}_2(\text{F})$ exhibited strong XRD diffraction peaks of sulfur, indicating that sulfur had penetrated into the interior of the two materials. The SEM image of $\text{S/CoNiO}_2(\text{B})$ (Figure S1) displays that the vulcanized composite maintains the polyhedral morphology, and the corresponding element mapping explains that the injected sulfur is evenly distributed. To inspect the interface and pore characteristics of $\text{CoNiO}_2(\text{B})$ and $\text{CoNiO}_2(\text{F})$, Brunauer–Emmett–Teller (BET) tests were carried out. Figure 2e clearly reveals that $\text{CoNiO}_2(\text{B})$ possesses a specific surface area of $204\text{ m}^2\text{ g}^{-1}$, which is larger than $\text{CoNiO}_2(\text{F})$ ($137\text{ m}^2\text{ g}^{-1}$), indicating that the architecture of the hollow nano-box is conducive to expansion of the specific surface area of the CoNiO_2 nano-compound. Figure 2f shows that the average pore-sizes of $\text{CoNiO}_2(\text{B})$ and $\text{CoNiO}_2(\text{F})$ are 17.356 nm and 34.563 nm, respectively. Although both materials have a mesoporous structure, $\text{CoNiO}_2(\text{B})$ has a larger specific surface area and smaller average pore-size, which can provide more active sites and efficient electron/ion transportation channels than $\text{CoNiO}_2(\text{F})$, which is beneficial for electrochemical performance of the Li-S batteries.

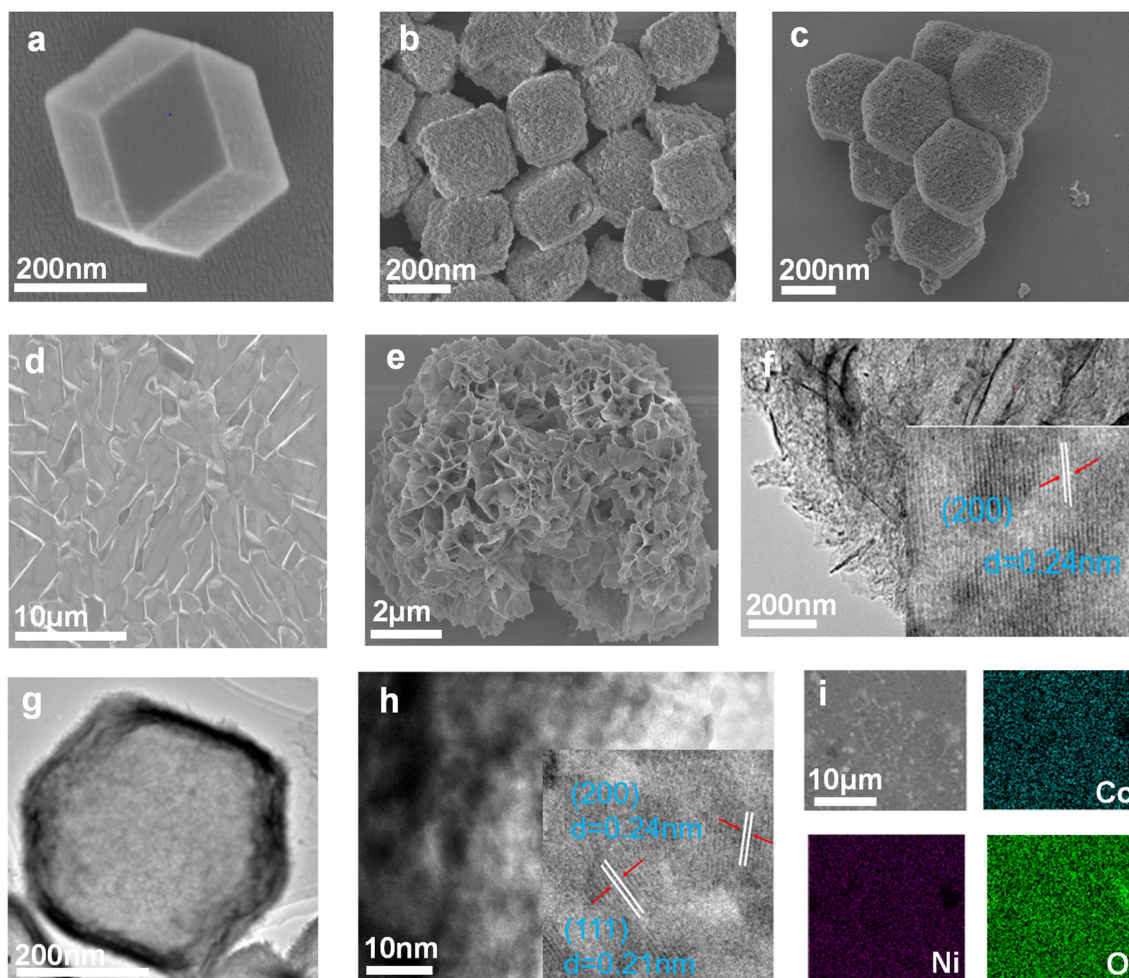


Figure 1. The SEM and TEM images. The SEM image of (a) ZIF-67, (b) NiCo-LDH(B), (c) CoNiO₂(B), (d) NiCo-LDH(F), and (e) CoNiO₂(F). TEM images of (f) CoNiO₂(F) and (g) CoNiO₂(B). (h) HRTEM images of CoNiO₂(B). (i) EDS elemental mapping of CoNiO₂(B).

Sulfur is injected into the host by melt-diffusion, and the mass proportion of sulfur was obtained from a thermogravimetric analysis (TGA) measurement. Due to sublimation of sulfur, the TGA curve has a large weight drop in the temperatures ranging from 200 °C to 350 °C, and the weight loss reflects the mass percentage of the loaded sulfur, as displayed in Figure 3a. S/CoNiO₂(B) has a higher sulfur content (72.4 wt%) than S/CoNiO₂(F) (69.9 wt%). This can be attributed to the large internal storage capacity of the hollow architecture of the CoNiO₂(B) material. In order to characterize the lithium hexasulfide-adsorption of the materials, 8 mg of the obtained NiCo-LDH(B), CoNiO₂(F), and CoNiO₂(B) were respectively soaked into 4 mL of 5 mM Li₂S₆ solution with a mixture solvent of DOL and DOE (volume ratio V/V = 1/1); their corresponding containing bottles were labeled as bottle 2, bottle 3, and bottle 4, while the bottle containing pure Li₂S₆ solution was labeled as bottle 1. All the solutions rested for 10 h. Figure 3b shows the results of the visualized static Li₂S₆ adsorption. It is clearly observed that bottle 4 has the highest transparency, followed by bottle 3, and finally bottle 2. Among them, the solution containing CoNiO₂(B) is almost colorless, indicating that CoNiO₂(B) has an excellent adsorption capacity for PSs. UV-vis spectra also confirmed the same conclusion, as the solution containing CoNiO₂(B) has the weakest absorption peak at the characteristic wavelength position of LiPSs [35].

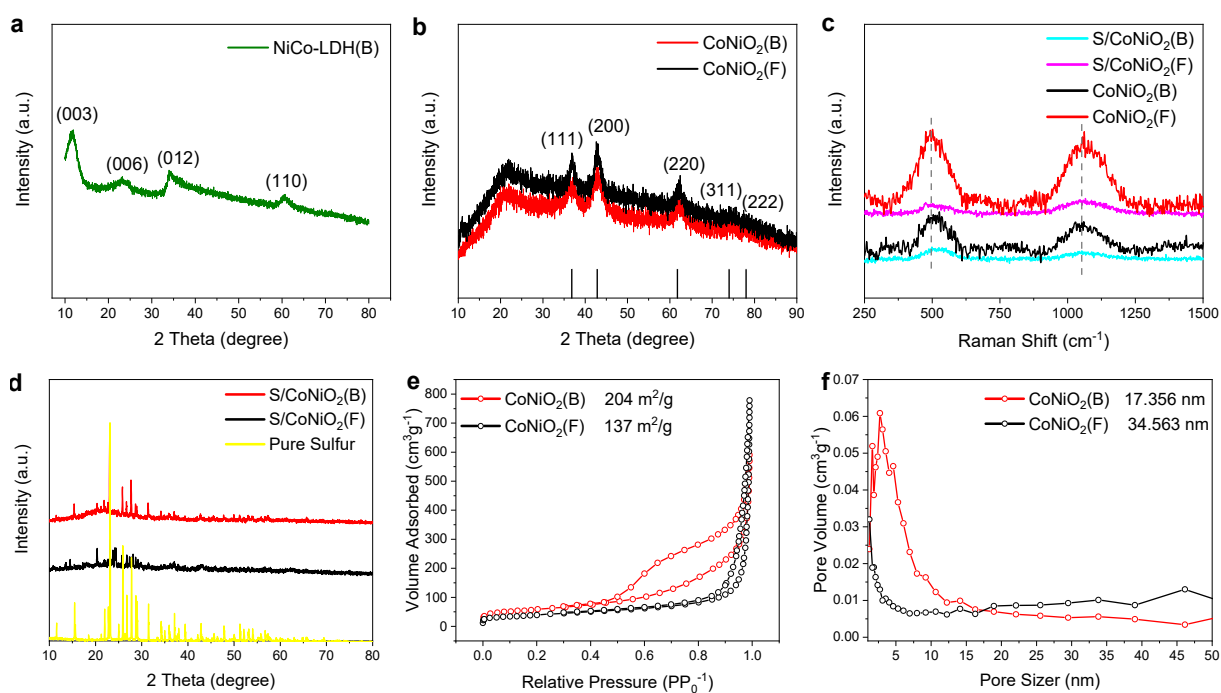


Figure 2. The result of XRD, Raman and BET; (a) X-ray diffraction pattern of NiCo-LDH(B). (b) XRD pattern of CoNiO₂(B) and CoNiO₂(F). (c) Raman spectra of CoNiO₂(B) and CoNiO₂(F). (d) XRD pattern of S/CoNiO₂(B) and S/CoNiO₂(F). (e) The isotherms of N₂ adsorption-desorption and (f) the distributions of pore sizes in CoNiO₂(B) and CoNiO₂(F).

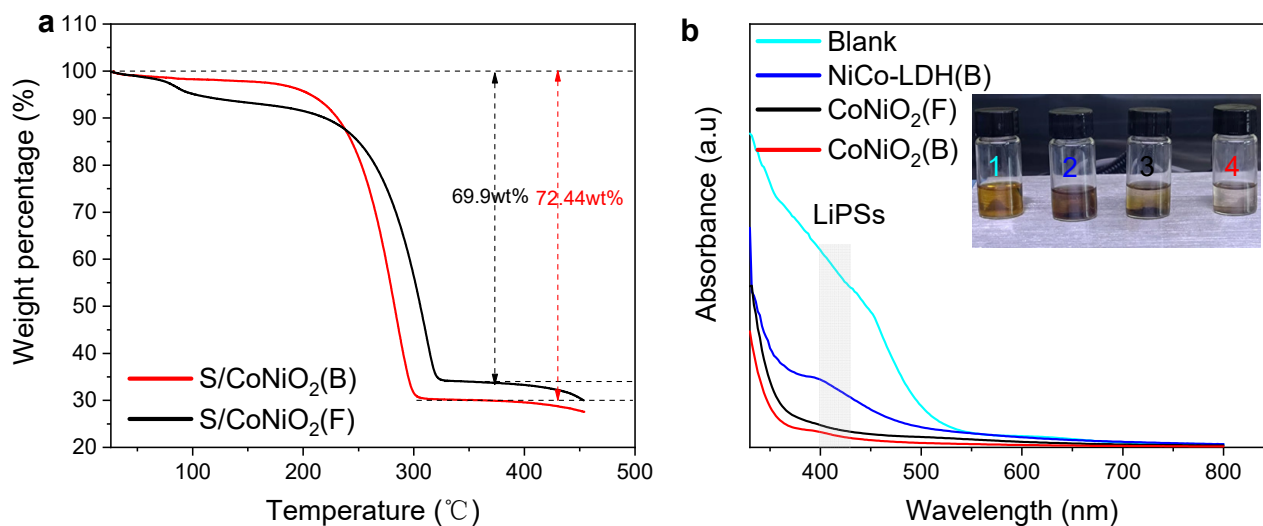


Figure 3. TGA and adsorption measurement; (a) TGA curve of S/CoNiO₂(B) and S/CoNiO₂(F). (b) UV/vis adsorption spectra and static adsorption images.

X-ray photoelectron spectroscopy (XPS) surveys were performed to explore the chemical state of the materials. The XPS full range binding energy spectrum (Figure S2) shows that CoNiO₂(B) and CoNiO₂(F) all contain the four elements Co, Ni, O, and C; the residual C may come from the ZIF-67 template or from environmental contamination. Figure 4a–c shows the photoelectron spectra of Co 2p, O 1s and Ni 2p in CoNiO₂(B). The Co 2p photoelectron spectroscopy in Figure 4a is split into two bands of Co 2p_{3/2} and Co 2p_{1/2}. The three subpeaks of the Co 2p_{3/2} band at 781.52 eV, 779.50 eV, and 785.94 eV are attributed to Co²⁺, Co³⁺, and satellite peaks, respectively. The Co 2p_{1/2} band can be deconvoluted into three peaks at 796.94 eV, 795.36 eV, and 802.32 eV, arising from Co²⁺, Co³⁺, and satellite

peaks, respectively [36]. In Figure 4b, the two fitting peaks of O 1s are located at 529.59 eV and 531.36 eV, which are severally related with O^{2-} and hydroxide [37]. Doublet bands of Ni 2p_{3/2} and Ni 2p_{1/2} constitute the XPS spectrum of Ni 2p (Figure 4c). Ni 2p_{3/2} and Ni 2p_{1/2} can be deconvoluted into Ni³⁺ (855.70 eV, 873.47 eV), Ni²⁺ (853.80 eV, 871.74 eV), and satellite peaks (860.91 eV, 879.08 eV) [38]. Figure 4d–f reveals the photoelectron spectra of Co 2p, O 1s, and Ni 2p in CoNiO₂(F). The Co 2p photoelectron spectrum in Figure 4d contains the two spin splitting peaks Co 2p_{3/2} (779.19 eV, 781.06 eV) and Co 2p_{1/2} (794.89 eV, 796.56 eV) as well as satellite peaks (785.59 eV, 801.97 eV), indicating the presence of Co²⁺ and Co³⁺ [36]. In Figure 4e, the two peaks (529.21 eV, 530.73 eV) in the XPS spectrum of O 1s individually correlated with O^{2-} and the hydroxyl groups [37]. In the XPS spectrum of Ni 2p (Figure 4f), there are four peaks at 853.52 eV, 855.22 eV, 871.17 eV, and 872.83 eV, belonging to Ni³⁺ 2p_{3/2}, Ni²⁺ 2p_{3/2}, Ni²⁺ 2p_{1/2}, and Ni³⁺ 2p_{1/2}, while those positioned at 860.66 eV and 878.70 eV represent the satellite peaks of Ni 2p [38]. From the above results of the XPS analysis, it can be concluded that CoNiO₂(B) and CoNiO₂(F) possess almost the same chemical status except the upshift of the binding energy of the former. Due to the attenuation of the curvature radius from the nano-flake to the nano-box, the material surface will generate corresponding internal stress [39]. Deng et al. [40] found that compared with solid nanowires, hollow nanotubes exhibit higher tensile strength. The upshift of the XPS spectrum is a fingerprint signal of the occurrence of tensile strain inside the material. Zhou et al. [41] have proved that the existence of the tensile strain results in the lattice deformation of materials, which makes the spectrum of XPS shift toward the direction of the high binding energy. Although the lattice deformation is so trifling that XRD test did not detect its existence, the XPS spectra of Co, Ni, and O elements presented above are a shift toward the direction of high binding energy, which is circumstantial evidence of the existence of tensile strain in the hollow architecture of CoNiO₂(B) [42].

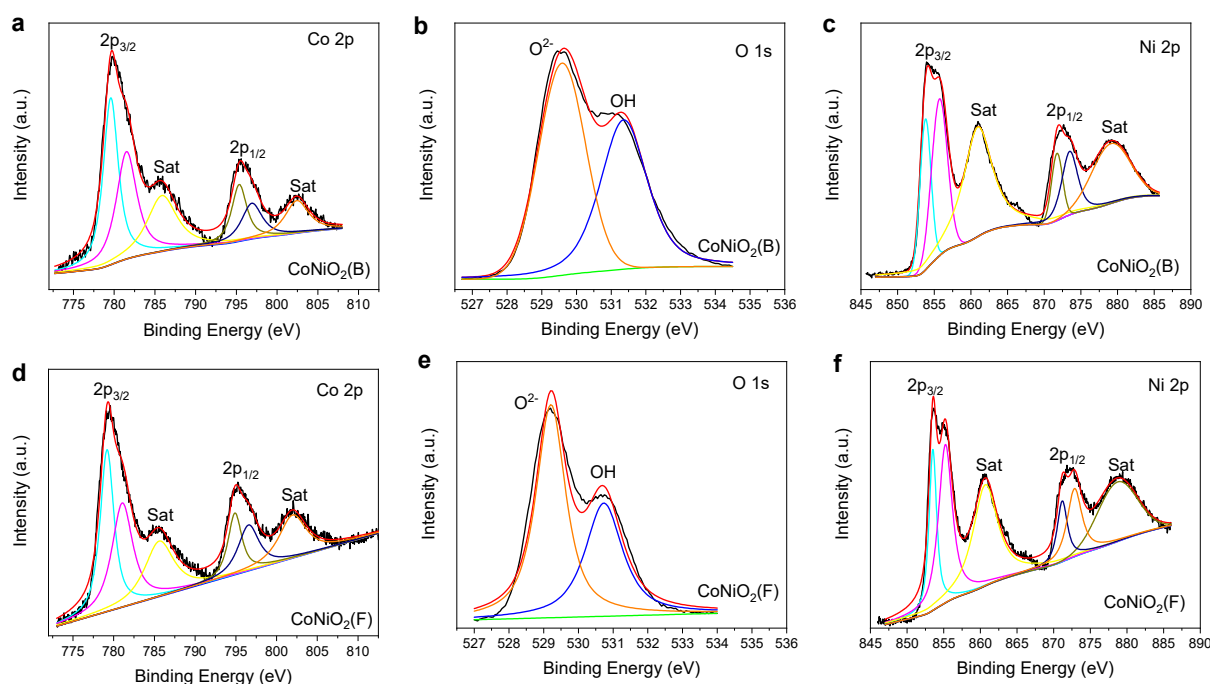


Figure 4. XPS spectra of CoNiO₂(B) and CoNiO₂(F). (a) Co 2p, (b) O 1s, and (c) Ni 2p XPS spectra of CoNiO₂(B). (d) Co 2p, (e) O 1s, and (f) Ni 2p XPS spectra of CoNiO₂(F).

In order to detect the chemical valence of sulfur injected into the material, the S 2p spectra in S/CoNiO₂(B) are shown in Figure S3a. The peaks at 163.4 eV and 164.56 eV can be assigned to the S 2p_{3/2} and S 2p_{1/2} of the chemical bonds towards S₈. S-O species (168.37 eV, 169.53 eV) are observed in the S/CoNiO₂(B) [43]. In Figure S3b, the S 2p peaks (163.18 eV and 164.34 eV) of S/CoNiO₂(F) are also attributed to S 2p_{3/2} and S 2p_{1/2},

and peaks (168.39 eV, 169.55 eV) are consistent with S-O species [43]. It can be concluded that the sulfur in S/CoNiO₂(B) and S/CoNiO₂(F) exists in two forms: pure sulfur and the combination between sulfur and CoNiO₂.

During the charging and discharging process, a rapid conversion of PSs can significantly minimize the shuttle effect. The effects of CoNiO₂(B) and CoNiO₂(F) on the liquid–liquid and solid–liquid conversion of PSs was measured by a symmetric cell. The CoNiO₂(B) symmetric cell without Li₂S₆ in Figure 5a produced nearly zero capacitive current, while the CoNiO₂(B) symmetric cell with Li₂S₆ electrolyte exhibited more than twice the redox current than CoNiO₂(F), indicating that CoNiO₂(B) vigorously accelerates the redox kinetics of the liquid–liquid conversion of PSs [44]. EIS spectra (Figure 5b) showed that CoNiO₂(B) symmetric cells exhibit lower charge transfer resistance (R_{ct}), further confirming that CoNiO₂(B) could promote redox reaction kinetics of PSs. The deposition of Li₂S represents the conversion of soluble PSs to insoluble Li₂S (liquid–solid). As exhibited in Figure 5c, the onset of Li₂S deposition is located at the upward inflection point of the potentiostatic discharge curve. The initial deposition time of Li₂S on CoNiO₂(B) is 897 s, which is earlier than that of CoNiO₂(F) at 1831.2 s. The peak current of CoNiO₂(B) is 0.430 A g⁻¹, which is larger than the 0.211 A g⁻¹ of CoNiO₂(F). The shorter Li₂S deposition time and the larger peak current confirm that CoNiO₂(B) can efficiently boost the transition of soluble PSs to solid Li₂S [45]. The excellent kinetic promotion of CoNiO₂(B) is predominantly attributed to the increased active site density and shortened path lengths for mass and ion transportation. Furthermore, the tensile strain that resulted from hollow architecture, as discussed above, is additionally beneficial for improvement of catalytic performance. Liu et al. [46] confirm that slight lattice deformation aroused from the tensile strain will result in lengthened chemical bonds, which will exert adjustment on the crystalline electronic structure. Wang et al. [47] demonstrated that, with tensile strain, the d-band center of the transition metal atom in the active sites shifts toward the Fermi level, thus improving the chemical adsorption and catalytic conversion of the PSs for further performance enhancement of Li-S batteries.

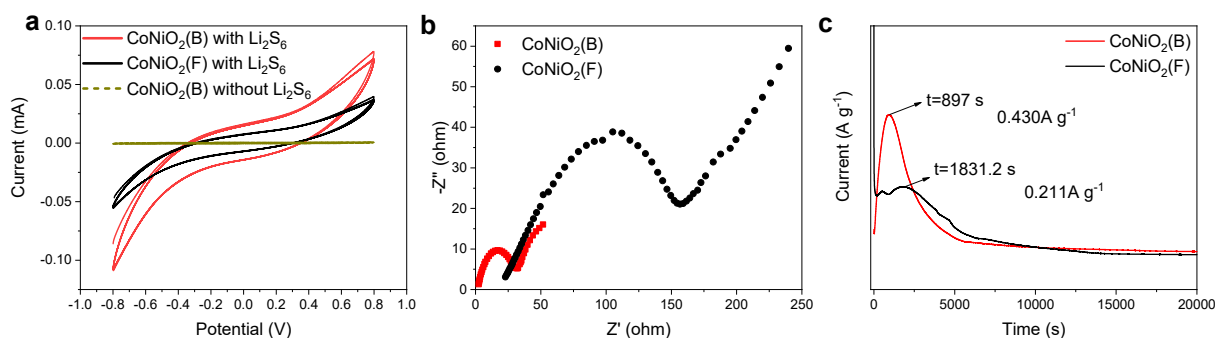


Figure 5. Electrochemical Performance of Symmetric Battery; (a) CV cycle curves and (b) EIS curves of CoNiO₂(B) and CoNiO₂(F) symmetric cells. (c) Li₂S deposition profiles on CoNiO₂(B) and CoNiO₂(F).

A coin battery was assembled for the cyclic voltammetry (CV) cycle testing to inspect the electrochemical reactivity of the Li-S battery. The CV curves of the S/CoNiO₂(B) and S/CoNiO₂(F) electrodes were examined at a scanning rate of 0.1 mV/s, and the results are displayed in Figure 6a. Within the voltage range of 1.7–2.8 V, there are two cathodic peaks (2.27 V, 2.01 V), which reflect the reaction that occurs during discharge—sulfur is reduced to soluble PSs, and soluble PSs are further reduced to solid state lithium sulfide. The anodic peak (2.42 V) signifies the oxidation of dilithium sulfide to sulfur during charging. The S/CoNiO₂(B) electrode exhibits a significantly larger peak current and narrower peak width, which indicates that CoNiO₂(B) enhances the charge–discharge reaction kinetics of PSs. In addition, charge–discharge reaction kinetics can be further analyzed by CV. The results of CV at five different scan rates are shown in Figure 6b–c. As the Randles–Sevcik principle points out, with the square root of the scanning rate and the peak current of the

CV curve as variables, the slope of the fitted curve between them reflects the Li^+ diffusion coefficient [48]. In general, the higher the slope, the faster the diffusion of Li^+ . Figure 6d–f show that the slopes of the fitted curves for the S/CoNiO₂(B) cathode at peak A, peak C₁, and peak C₂ are numerically larger than those for the S/CoNiO₂(F) cathode. The results verify that CoNiO₂(B) provides more channels and reduced path lengths for mass and ion transportation in the redox reaction.

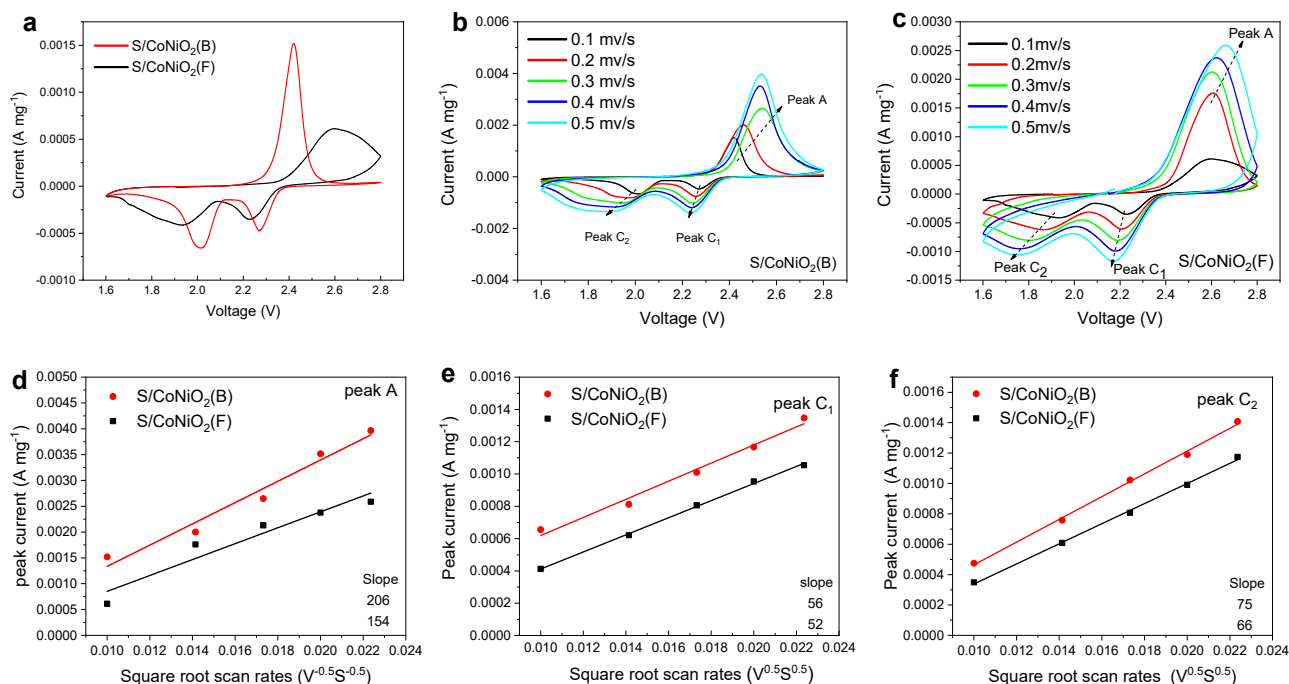


Figure 6. CV curves and Li^+ diffusion coefficient fitting. (a) CV curves of S/CoNiO₂(B) and S/CoNiO₂(F) electrode at 0.1 mV s⁻¹. CV curves of (b) S/CoNiO₂(B) and (c) S/CoNiO₂(F) electrode at 0.1–0.5 mV s⁻¹. (d–f) The peak current of the CV curve is linearly related to the square root of the corresponding scan rate.

All assembled coin batteries were aged at 50 °C for 48 h for activation before charge and discharge. Figure 7a shows galvanostatic charge–discharge profiles of the batteries with S/CoNiO₂(B) and S/CoNiO₂(F) cathodes for the initial three cycles at 0.05 C. The S/CoNiO₂(B) cathode exhibits one plateau near 2.39 V related to sulfur oxidation and two stages at 2.26 V and 2.10 V correlated with sulfur reduction, while the S/CoNiO₂(F) cathode exhibits one oxidation peak at 2.40 V and two reduction peaks at 2.24 V and 2.10 V. The charging–discharging overpotential of S/CoNiO₂(B) is 0.13 V, lower than that of S/CoNiO₂(F) (0.16 V), which denotes slighter polarization of the CoNiO₂(B) host. The discharge specific capacities of S/CoNiO₂(B) corresponding to the first, second, and third cycles are 1232 mAh g⁻¹, 1215 mAh g⁻¹, and 1190 mAh g⁻¹, respectively, which are all larger than S/CoNiO₂(F) (894 mAh g⁻¹, 869 mAh g⁻¹, 849 mAh g⁻¹). The 0.5 C rate cycling characteristics of the two type cathodes were revealed in Figure 7b. The first 25 cycles are conducted at current density of 0.05, 0.1, 0.2, 0.5 and 1 C. The first discharge specific capacity of the S/CoNiO₂(B) cathode decreased to 822 mAh g⁻¹, while a stable value of 730 mAh g⁻¹ remained after 150 cycles, which is 50% greater than the S/CoNiO₂(F) cathode (486 mAh g⁻¹). Figure 7c further reveals the rate performance of the S/CoNiO₂(B) cathode, which delivered an initial specific capacity of 931.2 mAh g⁻¹, 836.72 mAh g⁻¹, 736.82 mAh g⁻¹, 655 mAh g⁻¹, and 502.1 mAh g⁻¹ at a current density of 0.1, 0.2, 0.5, 1, and 2 C, respectively. When the current density suddenly decreased from 2 C to 0.2 C or 0.1 C, the reversible specific capacity can still be maintained at 757 mAh g⁻¹ and 807.441 mAh g⁻¹, respectively.

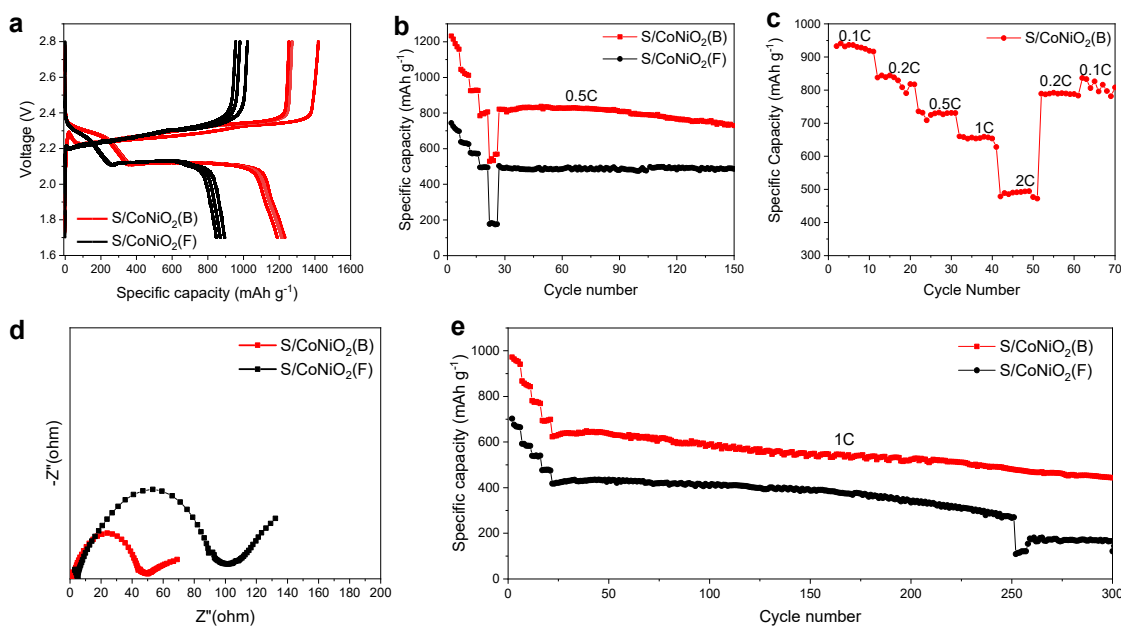


Figure 7. The electrochemical measurement of S/CoNiO₂(B) and S/CoNiO₂(F); (a) The voltage plateau curve of the S/CoNiO₂(B) electrode at 0.05 C in initial three cycles. (b) Cycle performances of the S/CoNiO₂(B) and S/CoNiO₂(F) electrode at 0.5 C. (c) Rate performances of the S/CoNiO₂(B) electrode. (d) EIS curves and (e) cycle performances at 1 C for the S/CoNiO₂(B) and S/CoNiO₂(F) electrode.

The electrochemical impedance spectra (EIS) of S/CoNiO₂(B) and S/CoNiO₂(F) cathodes are presented in Figure 7d. At the interface between electrolyte and cathode, the resistance of charge transfer is equivalent to the length from the coordinate origin to the right inflection point of the semicircle. The smaller impedance shows that the CoNiO₂(B) compound exhibits excellent electrochemical conductivity and diffusion kinetics. Long term cycle stability is an important evaluation index of Li-S battery performance. In order to study the effect of sulfur loading on battery performance, sulfur loading was accurately regulated at 1.6 mg cm⁻². When operated under 1 C rate, the initial specific capacity of the CoNiO₂(B) cathode maintained 631 mAh g⁻¹, while the CoNiO₂(F) cathode was only 421 mAh g⁻¹, as represented in Figure 7e. For the first 20 cycles, the current density gradually increases from 0.05, 0.1, 0.2, to 0.5C. After 300 cycles, their specific capacities were maintained at 431 mAh g⁻¹ and 121 mAh g⁻¹, respectively, and the CoNiO₂(B) was almost three times higher than CoNiO₂(F). Within 300 cycles, the capacity decay rate of the S/CoNiO₂(B) cathode was 0.1% per cycle, which is remarkably lower than that of the S/CoNiO₂(F) cathode (0.26%). The cycling stability of the S/CoNiO₂(B) electrode is preferable to the S/CoNiO₂(F) cathode.

Except for the fact that CoNiO₂(B) shows higher binding energy, CoNiO₂(B) and CoNiO₂(F) exhibit the same chemical status. However, the electrochemical performance of CoNiO₂(B) is much better than that of CoNiO₂(F). When material transforms from two-dimensional nano-flakes to three-dimensional nano-boxes, the specific surface area is enlarged, and slight internal tensile strain is generated [39]. The increase of the specific surface area not only exposes more active sites, but also provides more channels and reduced path lengths for mass and ion transportation. These effects are conducive to the performance improvement of Li-S batteries. In addition, due to the slight lattice deformation resulting from tensile strain in the material, chemical bonds are lengthened, which leads to the upshift of binding energy [46]. The lengthened chemical bonds will also exert effects on the electronic structure of the crystal; that is, the d-band center of the transition metal in the active sites will migrate toward the Fermi level, which will promote the chemical adsorption and catalytic conversion of the PSs for further performance enhancement of Li-S

batteries [47]. It can be asserted that, for the transition metal oxide compound, the hollow architecture is more promising than the two-dimensional analogues for the applications as sulfur host in Li-S batteries.

3. Materials and Methods

3.1. Material Preparation

Cobalt nitrate hexahydrate and nickel nitrate hexahydrate were analytical grade and produced by Damao Chemical Reagent Factory. 2-methylimidazole(2-MeIM) and Li_2S were purchased from Macklin Biochemical Co., Ltd. in Shanghai, China. Methanol, ethanol, and urea were purchased from XiLong Science Co., Ltd. in Guangdong, China. The sulfur was made by Heng Xing Chemical Reagent Manufacturing Co., Ltd. in Tianjin, China.

3.1.1. Synthesis of ZIF-67

2 mmol of cobalt nitrate hexahydrate was added to anhydrous methanol (50 mL), and the resulting solution after ultrasonic dispersion is solution A. 0.657 g of 2-MeIM (8 mmol) was completely dispersed in 50 mL of anhydrous methanol by sonication to get solution B. Solution A was forcefully stirred (>500 rpm), and solution B was rapidly added to solution A, then stirred for one minute and stewed 24 h. Finally, the purple product was rinsed with methanol 3–4 times and dried overnight in a 70 °C oven.

3.1.2. Synthesis of NiCo-LDH

20 mg of prepared ZIF-67 was dissolved in 20 mL ethanol to gain solution A. 100 mg of nickel nitrate hexahydrate was completely dispersed in 20 mL ethanol to get solution B. Solution A was stirred (>500 rpm), and solution B was quickly poured into solution A, continually stirred for 2 min. Then, the mixture was treated by ultrasonic treatment at room temperature with a power of 600 W for 1 h. Lastly, it was rinsed three to four times with ethanol before drying at 70 °C overnight.

3.1.3. Synthesis of NiCo-LDH(F)

Nickel nitrate hexahydrate (9 mmol), cobalt nitrate hexahydrate (4.5 mmol), and urea (31.5 mmol) were dissolved in 35 mL methanol. The mixture was stirred vigorously to form a transparent solution, then the transparent solution was poured into a 100 mL polytetrafluoroethylene lined stainless steel reaction kettle. Then, the reaction kettle was heated from room temperature to 120 °C at a rate of 5 °C/min and steeped for 10 h. Finally, NiCo-LDH(F) was obtained by washing and drying the mixture in the reaction kettle.

3.1.4. Synthesis of the $\text{CoNiO}_2(\text{B})/\text{CoNiO}_2(\text{F})$

The prepared 50 mg NiCo-LDH was annealed at 300 °C for 120 min with argon gas. The final product was $\text{CoNiO}_2(\text{B})$. The $\text{CoNiO}_2(\text{F})$ material was prepared from NiCo-LDH(F) by the same process.

3.1.5. Synthesis of the S/ $\text{CoNiO}_2(\text{B})$ and S/ $\text{CoNiO}_2(\text{F})$ Composite

$\text{CoNiO}_2(\text{B})$ and sulfur were mixed in 1:3 weight ratio and uniformly stirred for 5 h. Then, the product was heated at 155 °C for 6 h in a sealed autoclave for the preparation of S/ $\text{CoNiO}_2(\text{B})$. S/ $\text{CoNiO}_2(\text{F})$ composites were also obtained by the identical procedure.

3.2. Visualized Adsorption of Li_2S_6

To create a 5 mM Li_2S_6 solution, S and Li_2S powder (1:5 moles) were dissolved in a mixed solution of 1,3 dioxolane and 1,2-dimethoxyethane (1:1 volume) and stirred vigorously at 70 °C for 24 h. Then, 8 mg each of the NiCo-LDH, $\text{CoNiO}_2(\text{F})$, and $\text{CoNiO}_2(\text{B})$ were soaked in the prepared Li_2S_6 solution (4 mL) for 10 h.

3.3. Assembly of Symmetric Cells

The two hosts $\text{CoNiO}_2(\text{B})$ and $\text{CoNiO}_2(\text{F})$ were separately dissolved in absolute ethanol and sonicated for 60 min. The resultant homogeneous suspension was added dropwise to 12 mm discs of aluminum foil and dried quickly. The symmetrical battery was assembled by two identical electrodes into a 2025 coin battery with Celgard 2400 as the separator and an electrolyte containing 0.42 M Li_2S_6 . The electrolyte also included 1.0 mol/L lithium bis-trifluoromethanesulfonimide and 2% lithium nitrate, and equal amounts of 1,3-dioxolane and 1,2-dimethoxyethane. The CV curve scanning voltage range of the symmetrical battery ranged from -0.8 to 0.8 V at 200 mV/s. The corresponding EIS curves were measured by a Corrtest CS350H electrochemical workstation at 10^{-2} – 10^5 Hz with an amplitude of 5 mV.

3.4. Nucleation of Li_2S

The 2025 coin battery was assembled with $\text{CoNiO}_2(\text{B})$ as the cathode (or $\text{CoNiO}_2(\text{F})$), Li foil as the anode, and Celgard 2400 as the separator, and contained 0.3 M Li_2S_8 electrolyte. The electrolyte also contained 1.0 mol/L lithium bis-trifluoromethanesulfonimide and 2% lithium nitrate, and equal amounts of 1,3-dioxolane and 1,2-dimethoxyethane. The assembled battery was first discharged with constant current to 2.10 V at 0.110 mA and subsequently with the voltage at 2.09 V until the current was almost zero.

3.5. Material Characterization

The microscopic structure and morphological features of the composite material were characterized by cold field emission scanning electron microscope (SEM, ZEISS Sigma 300, 3 kv) and transmission electron microscopy (TEM, JEOL JEM 2100, 200 KV). The mass of sulfur in the cathode was measured by thermogravimetric analysis (TGA) in the N_2 atmosphere from 20 to 500 °C. Raman spectroscopy was measured with a 532 nm laser. The N_2 adsorption-desorption isotherm measurement was used to determine the Brunauer–Emmett–Teller (BET) surface area, and the diameter of pores was calculated from the BJH method (MicrotracBEL Corp). X-ray diffraction (XRD) spectra were measured by a D8 Advance diffractometer. X-ray photoelectron spectroscopy (XPSs, ESCALAB250xi) measurements were designed to detect the chemical forms of elements in materials, and Shirley fitting background type was selected for the XPS test data. UV/vis absorption spectra were measured by Agilent Technologies Cary 60 UV-Vis (G6860A).

3.6. Assembly of the Li-S Batteries and Measurements

The S/ $\text{CoNiO}_2(\text{B})$ (or S/ $\text{CoNiO}_2(\text{F})$), carbon black, and polyvinylidene fluoride were mixed with a weight ratio of 7:2:1. The N-methylpyrrolidinone was added to the mixture, and the mixture turned into a slurry under prolonged stirring. The slurry was evenly coated on the dark side of aluminum foil and dried at 60 °C. 2025 Coin cells were constructed with the S cathode, lithium foil anode, and a Celgard 2400 separator. The electrolyte was 1.0 mol/L lithium bis-trifluoromethanesulfonimide and 2% lithium nitrate, which dissolved in equal parts 1,3-dioxolane and 1,2-dimethoxyethane. The cathode was loaded with 1.0–1.6 mg cm^{-2} of sulfur. The amount of electrolyte was controlled at $E/S = 30 \mu\text{L mg}^{-1}$. The galvanostatic charge–discharge was measured by Neware battery test devices with the cut-off voltage of 1.7–2.8 V. EIS and CV were measured by a CorrTest CS350H Electrochemical Workstation. The amplitude of the EIS spectra was 5 mV, and the frequency was arranged from 10^{-1} Hz to 10^5 Hz. The CV cycling curves were scanned at 0.1 to 0.5 mV s^{-1} .

4. Conclusions

In this work, we explored the effects of the catalyst architecture on the cathodic performance of Li-S batteries. Dual transition metal oxide CoNiO_2 compound was selected as the conceptual material to synthesize three-dimensional hollow $\text{CoNiO}_2(\text{B})$ and two-dimensional $\text{CoNiO}_2(\text{F})$. As sulfur host, cells with a cathode comprised of nano-boxes delivered a of 1232 mAh g^{-1} and a low overpotential of 0.13 V at 0.05 C, as well as a cycle

stability with decay rate of 0.1% per cycle even after 300 cycles at 1 C, which are superior to two-dimensional analogues. The experiments imply that CoNiO₂(B) exhibits strong affinity toward PSs and excellent catalytic activity for the PSs redox kinetics compared with CoNiO₂(F). The enlarged specific surface area that resulted from the hollow architecture of the nano-box affords not only more active sites but also more channels and reduced path lengths for fast mass and ion transportation, which are conducive to performance enhancement of Li-S batteries. Additionally, the tensile strain aroused from the attenuated curvature radius from nano-flake to nano-box is another advantageous factor for performance enhancement, as tensile strain drives the d-band center of the transition metal in the active sites to migrate toward the Fermi level, which will promote the chemical adsorption and catalytic conversion of the PSs. Our research has demonstrated that catalysts with hollow architecture are more promising than their two-dimensional analogues in practical application in the Li-S batteries.

Supplementary Materials: The following supporting information can be downloaded at <https://www.mdpi.com/article/10.3390/batteries8120262/s1>. Figure S1: (a) The SEM image of S/CoNiO₂(B), (b) EDS elemental mapping of S/CoNiO₂(B); Figure S2: The XPS survey spectrum of (a) CoNiO₂(B) and (b) CoNiO₂(F); Figure S3: S 2p XPS spectra of (a) S/CoNiO₂(B) and (b) S/CoNiO₂(F).

Author Contributions: Conceptualization, Y.Z.; methodology, L.Q.; software, X.L.; formal analysis, Z.H.; investigation, F.L.; resources, Z.Z.; data curation, H.Y.; writing—original draft preparation, L.C.; funding acquisition, L.W. All authors have read and agreed to the published version of the manuscript.

Funding: This research was funded by [Yong Zhao] grant number [No. 12175098]. And the APC was funded by [No. 12175098].

Institutional Review Board Statement: Not applicable.

Informed Consent Statement: Not applicable.

Data Availability Statement: Not applicable.

Acknowledgments: The authors acknowledge the financial support from the National Natural Science Foundation of China (No. 12175098).

Conflicts of Interest: The authors declare no conflict of interest.

References

1. Chung, S.; Chang, C.; Manthiram, A. Progress on the Critical Parameters for Lithium-Sulfur Batteries to be Practically Viable. *Adv. Funct. Mater.* **2018**, *28*, 1801188. [[CrossRef](#)]
2. Fang, X.; Peng, H. A Revolution in Electrodes: Recent Progress in Rechargeable Lithium-Sulfur Batteries. *Small* **2015**, *11*, 1488–1511. [[CrossRef](#)]
3. Salama, M.; Rosy; Attias, R.; Yemini, R.; Gofer, Y.; Aurbach, D.; Noked, M. Metal-Sulfur Batteries: Overview and Research Methods. *ACS Energy Lett.* **2019**, *4*, 436–446. [[CrossRef](#)]
4. Tu, S.; Chen, X.; Zhao, X.; Cheng, M.; Xiong, P.; He, Y.; Zhang, Q.; Xu, Y. A Polysulfide-Immobilizing Polymer Retards the Shuttling of Polysulfide Intermediates in Lithium-Sulfur Batteries. *Adv. Mater.* **2018**, *30*, e1804581. [[CrossRef](#)] [[PubMed](#)]
5. Wang, Y.; Zhang, R.; Pang, Y.-C.; Chen, X.; Lang, J.; Xu, J.; Xiao, C.; Li, H.; Xi, K.; Ding, S. Carbon@titanium nitride dual shell nanospheres as multi-functional hosts for lithium sulfur batteries. *Energy Storage Mater.* **2019**, *16*, 228–235. [[CrossRef](#)]
6. Liu, D.; Zhang, C.; Zhou, G.; Lv, W.; Ling, G.; Zhi, L.; Yang, Q.H. Catalytic Effects in Lithium-Sulfur Batteries: Promoted Sulfur Transformation and Reduced Shuttle Effect. *Adv. Sci.* **2018**, *5*, 1700270. [[CrossRef](#)] [[PubMed](#)]
7. Wang, L.; Lu, Y.; Ma, S.; Lian, Z.; Gu, X.; Li, J.; Li, Z.; Liu, Q. Optimizing CO₂ reduction and evolution reaction mediated by o-phenylenediamine toward high performance Li-CO₂ battery. *Electrochim. Acta* **2022**, *419*, 140424. [[CrossRef](#)]
8. Zeng, L.; Zhu, J.; Liu, M.; Zhang, P. Sb nanosheet modified separator for Li-S batteries with excellent electrochemical performance. *RSC Adv.* **2021**, *11*, 6798–6803. [[CrossRef](#)]
9. Yi, T.F.; Shi, L.; Han, X.; Wang, F.; Zhu, Y.; Xie, Y. Approaching High-Performance Lithium Storage Materials by Constructing Hierarchical CoNiO₂@CeO₂ Nanosheets. *Energy Environ. Mater.* **2021**, *4*, 586–595. [[CrossRef](#)]
10. Li, Z.; Yuan, L.; Yi, Z.; Sun, Y.; Liu, Y.; Jiang, Y.; Shen, Y.; Xin, Y.; Zhang, Z.; Huang, Y. Insight into the Electrode Mechanism in Lithium-Sulfur Batteries with Ordered Microporous Carbon Confined Sulfur as the Cathode. *Adv. Energy Mater.* **2014**, *4*, 1301473. [[CrossRef](#)]

11. Liu, J.; Xiao, S.H.; Zhang, Z.; Chen, Y.; Xiang, Y.; Liu, X.; Chen, J.S.; Chen, P. Naturally derived honeycomb-like N, S-codoped hierarchical porous carbon with MS₂ (M = Co, Ni) decoration for high-performance Li-S battery. *Nanoscale* **2020**, *12*, 5114–5124. [[CrossRef](#)] [[PubMed](#)]
12. Rehman, S.; Guo, S.; Hou, Y. Rational Design of Si/SiO₂@Hierarchical Porous Carbon Spheres as Efficient Polysulfide Reservoirs for High-Performance Li-S Battery. *Adv. Mater.* **2016**, *28*, 3167–3172. [[CrossRef](#)] [[PubMed](#)]
13. Ji, X.; Lee, K.T.; Nazar, L. A highly ordered nanostructured carbon-sulphur cathode for lithium-sulphur batteries. *Nat. Mater.* **2009**, *8*, 500–506. [[CrossRef](#)] [[PubMed](#)]
14. Liang, X.; Hart, C.J.; Pang, Q.; Garsuch, A.; Weiss, T.; Nazar, L.F. A highly efficient polysulfide mediator for lithium-sulfur batteries. *Nat. Commun.* **2015**, *6*, 5682. [[CrossRef](#)] [[PubMed](#)]
15. Li, Z.; Zhang, J.; Lou, X.W. Hollow Carbon Nanofibers Filled with MnO₂ Nanosheets as Efficient Sulfur Hosts for Lithium-Sulfur Batteries. *Angew. Chem. Int. Ed.* **2015**, *54*, 12886–12890. [[CrossRef](#)]
16. Li, Z.; Zhang, J.; Guan, B.; Wang, D.; Liu, L.-M.; Lou, X.W. A sulfur host based on titanium monoxide@carbon hollow spheres for advanced lithium-sulfur batteries. *Nat. Commun.* **2016**, *7*, 13065. [[CrossRef](#)]
17. Li, Z.; Guan, B.Y.; Zhang, J.; Lou, X.W. A Compact Nanoconfined Sulfur Cathode for High-Performance Lithium-Sulfur Batteries. *Joule* **2017**, *1*, 576–587. [[CrossRef](#)]
18. You, Y.; Ye, Y.; Wei, M.; Sun, W.; Tang, Q.; Zhang, J.; Chen, X.; Li, H.; Xu, J. Three-dimensional MoS₂/rGO foams as efficient sulfur hosts for high-performance lithium-sulfur batteries. *Chem. Eng. J.* **2019**, *355*, 671–678. [[CrossRef](#)]
19. Ye, C.; Zhang, L.; Guo, C.; Li, D.; Vasileff, A.; Wang, H.; Qiao, S. A 3D Hybrid of Chemically Coupled Nickel Sulfide and Hollow Carbon Spheres for High Performance Lithium-Sulfur Batteries. *Adv. Funct. Mater.* **2017**, *27*, 1702524. [[CrossRef](#)]
20. Pang, Q.; Kundu, D.; Nazar, L.F. A graphene-like metallic cathode host for long-life and high-loading lithium-sulfur batteries. *Mater. Horizons* **2016**, *3*, 130–136. [[CrossRef](#)]
21. Peng, H.-J.; Zhang, G.; Chen, X.; Zhang, Z.-W.; Xu, W.-T.; Huang, J.-Q.; Zhang, Q. Enhanced Electrochemical Kinetics on Conductive Polar Mediators for Lithium-Sulfur Batteries. *Angew. Chem.* **2016**, *128*, 13184–13189. [[CrossRef](#)]
22. Zhou, T.; Zhao, Y.; Zhou, G.; Lv, W.; Sun, P.; Kang, F.; Li, B.; Yang, Q.-H. An in-plane heterostructure of graphene and titanium carbide for efficient polysulfide confinement. *Nano Energy* **2017**, *39*, 291–296. [[CrossRef](#)]
23. Zhang, J.; Li, Z.; Chen, Y.; Gao, S.; Lou, X.W. Nickel-Iron Layered Double Hydroxide Hollow Polyhedrons as a Superior Sulfur Host for Lithium-Sulfur Batteries. *Angew. Chem. Int. Ed.* **2018**, *57*, 10944–10948. [[CrossRef](#)]
24. Qiu, W.; Li, G.; Luo, D.; Zhang, Y.; Zhao, Y.; Zhou, G.; Shui, L.; Wang, X.; Chen, Z. Hierarchical Micro-Nanoclusters of Bimetallic Layered Hydroxide Polyhedrons as Advanced Sulfur Reservoir for High-Performance Lithium-Sulfur Batteries. *Adv. Sci.* **2021**, *8*, 2003400. [[CrossRef](#)]
25. Yuan, Z.; Peng, H.-J.; Hou, T.-Z.; Huang, J.Q.; Chen, C.-M.; Wang, D.-W.; Cheng, X.-B.; Wei, F.; Zhang, Q. Powering Lithium-Sulfur Battery Performance by Propelling Polysulfide Redox at Sulfiphilic Hosts. *Nano Lett.* **2016**, *16*, 519–527. [[CrossRef](#)] [[PubMed](#)]
26. Zhang, J.; Hu, H.; Li, Z.; Lou, X.W.D. Double-Shelled Nanocages with Cobalt Hydroxide Inner Shell and Layered Double Hydroxides Outer Shell as High-Efficiency Polysulfide Mediator for Lithium-Sulfur Batteries. *Angew. Chem. Int. Ed.* **2016**, *55*, 3982–3986. [[CrossRef](#)]
27. Zhang, L.; Wan, F.; Cao, H.; Liu, L.; Wang, Y.; Niu, Z. Integration of Binary Active Sites: Co₃V₂O₈ as Polysulfide Traps and Catalysts for Lithium-Sulfur Battery with Superior Cycling Stability. *Small* **2020**, *16*, e1907153. [[CrossRef](#)]
28. Freund, L. Substrate curvature due to thin film mismatch strain in the nonlinear deformation range. *J. Mech. Phys. Solids* **2000**, *48*, 1159–1174. [[CrossRef](#)]
29. Zhang, C.; Chu, W.; Hong, X.; He, Q.; Lu, R.; Liao, X.; Zhao, Y. Accelerating conversion of LiPSs on strain-induced MXene for high-performance Li-S battery. *Chem. Eng. J.* **2022**, *439*, 135679. [[CrossRef](#)]
30. Li, J.; Qiu, W.; Liu, X.; Zhang, Y.; Zhao, Y. NiCo-Layered Double Hydroxide to Composite with Sulfur as Cathodes for High-Performance Lithium-Sulfur Batteries. *ChemElectroChem* **2022**, *9*, e202101211. [[CrossRef](#)]
31. Yang, J.; Yang, X.; Cheong, J.L.; Zaghbi, K.; Trudeau, M.L.; Ying, J.Y. Nanoboxes with a porous MnO core and amorphous TiO₂ shell as a mediator for lithium-sulfur batteries. *J. Mater. Chem. A* **2021**, *9*, 4952–4961. [[CrossRef](#)]
32. An, L.; Huang, B.; Zhang, Y.; Wang, R.; Zhang, N.; Dai, T.; Xi, P.; Yan, C. Interfacial Defect Engineering for Improved Portable Zinc-Air Batteries with a Broad Working Temperature. *Angew. Chem. Int. Ed.* **2019**, *58*, 9459–9463. [[CrossRef](#)]
33. Wang, W.; Lu, Y.; Zhao, M.; Luo, R.; Yang, Y.; Peng, T.; Yan, H.; Liu, X.; Luo, Y. Controllable Tuning of Cobalt Nickel-Layered Double Hydroxide Arrays as Multifunctional Electrodes for Flexible Supercapattery Device and Oxygen Evolution Reaction. *ACS Nano* **2019**, *13*, 12206–12218. [[CrossRef](#)]
34. Li, Z.; Mi, H.; Guo, F.; Ji, C.; He, S.; Li, H.; Qiu, J. Oriented Nanosheet-Assembled CoNi-LDH Cages with Efficient Ion Diffusion for Quasi-Solid-State Hybrid Supercapacitors. *Inorg. Chem.* **2021**, *60*, 12197–12205. [[CrossRef](#)] [[PubMed](#)]
35. Deng, D.-R.; Xue, F.; Jia, Y.-J.; Ye, J.-C.; Bai, C.-D.; Zheng, M.-S.; Dong, Q.-F. Co₄N Nanosheet Assembled Mesoporous Sphere as a Matrix for Ultrahigh Sulfur Content Lithium-Sulfur Batteries. *ACS Nano* **2017**, *11*, 6031–6039. [[CrossRef](#)]
36. Chen, F.-F.; Chen, J.; Li, L.; Peng, F.; Yu, Y. g-C₃N₄ microtubes@CoNiO₂ nanosheets p-n heterojunction with a hierarchical hollow structure for efficient photocatalytic CO₂ reduction. *Appl. Surf. Sci.* **2022**, *579*, 151997. [[CrossRef](#)]
37. Liu, Y.; Zhao, Y.; Yu, Y.; Ahmad, M.; Sun, H. Facile synthesis of single-crystal mesoporous CoNiO₂ nanosheets assembled flowers as anode materials for lithium-ion batteries. *Electrochim. Acta* **2014**, *132*, 404–409. [[CrossRef](#)]

38. Rehman, S.U.; Wang, J.; Luo, Q.; Sun, M.; Jiang, L.; Han, Q.; Liu, J.; Bi, H. Starfish-like C/CoNiO₂ heterostructure derived from ZIF-67 with tunable microwave absorption properties. *Chem. Eng. J.* **2019**, *373*, 122–130. [[CrossRef](#)]
39. Mézin, A. Coating internal stress measurement through the curvature method: A geometry-based criterion delimiting the relevance of Stoney's formula. *Surf. Coatings Technol.* **2006**, *200*, 5259–5267. [[CrossRef](#)]
40. Sun, M.; Xiao, F.; Deng, C. Near-ideal strength in metal nanotubes revealed by atomistic simulations. *Appl. Phys. Lett.* **2013**, *103*, 231911. [[CrossRef](#)]
41. Zhou, W.-P.; Lewera, A.; Bagus, P.S.; Wieckowski, A. Electrochemical and Electronic Properties of Platinum Deposits on Ru (0001): Combined XPS and Cyclic Voltammetric Study. *J. Phys. Chem. C* **2007**, *111*, 13490–13496. [[CrossRef](#)]
42. Clavel, M.B.; Hudait, M.K. Band Offset Enhancement of a-Al₂O₃/Tensile-Ge for High Mobility Nanoscale pMOS Devices. *IEEE Electron Device Lett.* **2017**, *38*, 1196–1199. [[CrossRef](#)]
43. Sun, W.; Liu, C.; Li, Y.; Luo, S.; Liu, S.; Hong, X.; Xie, K.; Liu, Y.; Tan, X.; Zheng, C. Rational Construction of Fe₂N@C Yolk-Shell Nanoboxes as Multifunctional Hosts for Ultralong Lithium-Sulfur Batteries. *ACS Nano* **2019**, *13*, 12137–12147. [[CrossRef](#)] [[PubMed](#)]
44. Sun, R.; Bai, Y.; Luo, M.; Qu, M.; Wang, Z.; Sun, W.; Sun, K. Enhancing Polysulfide Confinement and Electrochemical Kinetics by Amorphous Cobalt Phosphide for Highly Efficient Lithium-Sulfur Batteries. *ACS Nano* **2021**, *15*, 739–750. [[CrossRef](#)] [[PubMed](#)]
45. Chen, S.; Luo, J.; Li, N.; Han, X.; Wang, J.; Deng, Q.; Zeng, Z.; Deng, S. Multifunctional LDH/Co₉S₈ heterostructure nanocages as high-performance lithium-sulfur battery cathodes with ultralong lifespan. *Energy Storage Mater.* **2020**, *30*, 187–195. [[CrossRef](#)]
46. Zhou, D.; Wang, S.; Jia, Y.; Xiong, X.; Yang, H.; Liu, S.; Tang, J.; Zhang, J.; Liu, D.; Zheng, L.; et al. NiFe Hydroxide Lattice Tensile Strain: Enhancement of Adsorption of Oxygenated Intermediates for Efficient Water Oxidation Catalysis. *Angew. Chem. Int. Ed.* **2019**, *58*, 736–740. [[CrossRef](#)]
47. Wang, X.; Luo, D.; Wang, J.; Sun, Z.; Cui, G.; Chen, Y.; Wang, T.; Zheng, L.; Zhao, Y.; Shui, L.; et al. Strain Engineering of a MXene/CNT Hierarchical Porous Hollow Microsphere Electrocatalyst for a High-Efficiency Lithium Polysulfide Conversion Process. *Angew. Chem. Int. Ed.* **2021**, *60*, 2371–2378. [[CrossRef](#)]
48. He, J.; Hartmann, G.; Lee, M.; Hwang, G.S.; Chen, Y.; Manthiram, A. Freestanding 1T MoS₂/graphene heterostructures as a highly efficient electrocatalyst for lithium polysulfides in Li-S batteries. *Energy Environ. Sci.* **2019**, *12*, 344–350. [[CrossRef](#)]